

Cite this article as: Feng Ruicheng, Yang Shengze, Shao Zihao, et al. Atomistic Simulation of Effects of Random Roughness on Nano-cutting Process of γ -TiAl Alloy[J]. Rare Metal Materials and Engineering, 2022, 51(05): 1650-1659.

ARTICLE

Atomistic Simulation of Effects of Random Roughness on Nano-cutting Process of γ -TiAl Alloy

Feng Ruicheng^{1,2}, Yang Shengze¹, Shao Zihao¹, Yao Yongjun¹, Zhang Jun¹, Cao Hui¹, Li Haiyan^{1,2}

¹ School of Mechanical and Electronical Engineering, Lanzhou University of Technology, Lanzhou 730050, China; ² Key Laboratory of Digital Manufacturing Technology and Application, Ministry of Education, Lanzhou University of Technology, Lanzhou 730050, China

Abstract: The molecular dynamics simulations were conducted to investigate the effects of random roughness on nano-cutting of γ -TiAl alloys. To simulate the actual workpiece surface, the random surface roughness was generated by a multivariate Weierstrass-Mandelbrot (W-M) function under the condition of different rake angles of cutter and depths of cutting. The equivalent height of the workpiece was used to quantify the depth of cutting. The molecular dynamics simulation results reveal that the roughness has a profound effect on the nano-cutting quality of the workpiece. Besides, the effects of roughness are also different under different cutting parameters.

Key words: molecular dynamics; nano-cutting; W-M function; γ -TiAl alloy

TiAl alloys have a widespread application in the aviation industry and automobile industry due to their high strength, low density, and perfect high-temperature performance^[1,2]. However, it is difficult to achieve an acceptable machining accuracy for TiAl alloys at the micron or even larger scale due to the brittleness effect at room temperature^[3]. Meanwhile, the brittle materials have a ductile cutting mode when the depth of cutting (DOC) is small enough^[4]. Therefore, cutting or grinding of TiAl alloys at nanoscale is a promising method in ultra-precision machining^[5].

Although the precision cutting at nanoscale can be realized^[6], the high cost restricts its research in practice and application. Hence, the simulation method is widely used to investigate the precision cutting with acceptable cost and accurate results. Finite element method (FEM) and molecular dynamics (MD) simulations^[7] are commonly used methods to study the material removal process. As a special kind of peridynamics, MD is based on the nonlocal theory. According to the integral form of Newton's second law, all the deformation, such as crack initiation, can be identified as a spontaneous process^[8]. Meanwhile, MD can be used to explain

the microscopic mechanisms, such as the dislocation nucleation and fault slip. An et al^[9] observed the phase transition caused by the stacking of layers in the tension process of α -Ti alloy with stacking fault and analyzed the stacking fault evolution. Zhu et al^[10] researched the chip formation mechanism in the nano-cutting process of single-crystal nickel alloy and found that the cutting depth plays an important role in chip formation and surface flatness. Zhang et al^[11] adopted a quasi-continuum method of combination of MD and FEM to simulate the cutting process of copper alloy, and the slip band in the subsurface could be found. Saurav et al^[12] studied the cutting deformation response of polycrystal silicon material, and found that the amorphization is induced by stress instead of temperature.

However, most MD simulations are idealized, especially for the studies of machining with the hypothesis of smooth surface, which is impossible in the practical circumstance. Thus, the effect of roughness on cutting performance through MD simulation is barely investigated. Li et al^[13] analyzed the effects of temperature, shape, and direction of grinding on a regular rough crystal copper surface, and concluded that the

Received date: May 12, 2021

Foundation item: National Natural Science Foundation of China (52065036); Natural Science Foundation of Gansu Province (20JR5RA448); Hongliu First-Class Disciplines Development Program of Lanzhou University of Technology

Corresponding author: Feng Ruicheng, Ph. D., Professor, School of Mechanical and Electronical Engineering, Lanzhou University of Technology, Lanzhou 730050, P. R. China, Tel: 0086-931-5135199, E-mail: postfeng@lut.edu.cn

Copyright © 2022, Northwest Institute for Nonferrous Metal Research. Published by Science Press. All rights reserved.

machining parameters should be adjusted with the change of roughness. Michail et al^[14] explained the effects of the roughness of cutter and workpiece on the cutting force. It is reported that a high fractal dimension of the surface can enhance the cutting forces and reduce the energy efficiency. Nonetheless, the defects and deformation response are rarely investigated by MD through fractal theory.

In this research, a series of MD simulations were conducted to research the effects of roughness on nano-cutting process of γ -TiAl alloy. Firstly, the Weierstrass-Mandelbrot (W-M)^[15] function was applied to generate the surface of γ -TiAl alloy with different roughness. Secondly, the relationships between the machining parameters and defects were investigated with different values of DOC and roughness. Finally, the influence of rake angle was studied during the nano-cutting process. Because the roughness is just represented by the statistic value, the actual surface roughness of workpieces is not uniform. Hence, the effect of roughness was only studied qualitatively in this simulation.

1 Model and Methods

1.1 Crystallographic structure

As shown in Fig.1, the γ -TiAl alloy has an L_{10} face-centered

$$z(x,y) = C \sum_{m=1}^M \sum_{n=0}^{n_{\max}} \gamma^{(D_s - 3)n} \left\{ \cos \Phi_{m,n} - \cos \left[\frac{2\pi\gamma^n \sqrt{x^2 + y^2}}{L_{\max}} \cos \left(\tan^{-1} \left(\frac{y}{x} \right) - \frac{\pi m}{M} \right) + \Phi_{m,n} \right] \right\} \quad (1)$$

where M is the number of ridges; n_{\max} is the frequencies of ridges; n and m are the initial values of ridge number and frequency, respectively; γ represents the ratio of amplitude to frequency of the cosine shape, and γ is set as 1.5^[18]; D_s is the fractal dimension of 2~3^[19]; L_{\max} is the maximum size of the specimen; C is a scaling factor; $\Phi_{m,n}$ is a random matrix. In this research, a two-dimensional fractal profile was used as the ridge, and then the random surface was generated by the superposition of ridges with different angles and ranges in a cartesian coordinate system described by x , y , and z coordinates. The scaling factor C can be expressed as follows:

$$C = L_{\max} \left(\frac{G}{L_{\max}} \right)^{D_s - 2} \left(\frac{\ln \gamma}{M} \right)^{1/2} \quad (2)$$

where G is the roughness coefficient to indicate the surface amplitude. Theoretically, the fractal will be perfect if n approaches infinity. However, the value of n_{\max} can be calculated by Eq.(3), as follows:

$$n_{\max} = \text{int} \left[\frac{\lg(L_{\max}/L_{\min})}{\lg \gamma} \right] \quad (3)$$

where L_{\min} is the minimum size of the specimen. To quantify the surface roughness, the root-mean-square (RMS) of the surface roughness can be obtained by Eq.(4), as follows:

$$R_q = \sqrt{\frac{\sum_{i=1}^N z_i^2}{N}} \quad (4)$$

where z_i is the coordinate height of point i ; N is the number of points.

In this research, all the simulations were implemented by Large-scale Atomic/Molecular Massively Parallel Simulator

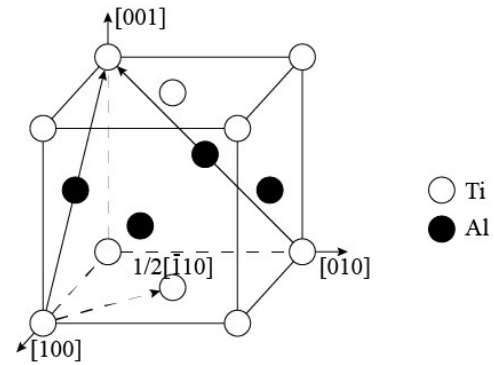


Fig.1 Crystal structure of γ -TiAl alloy

tetragonal (fct) structure^[16]. The x , y , and z axes correspond to the orientations of $[100]$, $[010]$, and $[001]$ in crystallography, respectively. In this simulation, the lattice constants a_0 , b_0 , and c_0 are 0.4001, 0.4001, and 0.4181 nm, respectively; while in the experiment, $a_0=b_0=0.4005$ nm and $c_0=0.40707$ nm^[17].

1.2 Random roughness generation

The multivariate W-M function^[15] can be used to generate the random roughness of surfaces, as follows:

(LAMMPS)^[20] software. However, there is no function in LAMMPS to generate the random roughness of surface. Thus, the additional script is required to complete the function. As shown in Fig.2, a series of coordinate points containing W-M function data were generated by the python script firstly. Then, a simple data file containing the work-blank was created by LAMMPS. Finally, after choosing a base plain, all the atoms in the data file would be checked whether their z coordinate values are higher than those of the corresponding point in the script. If their z coordinate values are higher, these atoms would be deleted.

1.3 Simulation parameters

The nano-cutting model in Fig.3 shows that the workpiece is divided into three layers: newton layer, thermostat layer, and boundary layer^[21]. The workpiece consists of single-crystal γ -TiAl alloy. The height in the z -direction of the workpiece is defined by the equivalent height, which corresponds to the median surface of the rough surface. Therefore, DOC is defined by the distance from the tool bottom to the median surface.

To qualitatively study the effects of roughness on nano-cutting process, three workpieces with RMS=0, 6.17, 9.59 and $G=0, 10^{-5}, 10^{-4}$ were generated. The fractal dimension is set as 2.2. Fig. 4 shows the three-dimensional diagrams of the workpieces with different values of RMS and the corresponding cross sections. The length in x -direction is 28.007 nm, the thickness in y -direction is 18 nm, while the equivalent height in z -direction is 10, 10.34, and 10.2 nm when RMS is 0, 6.17, and 9.59, respectively. The cutting

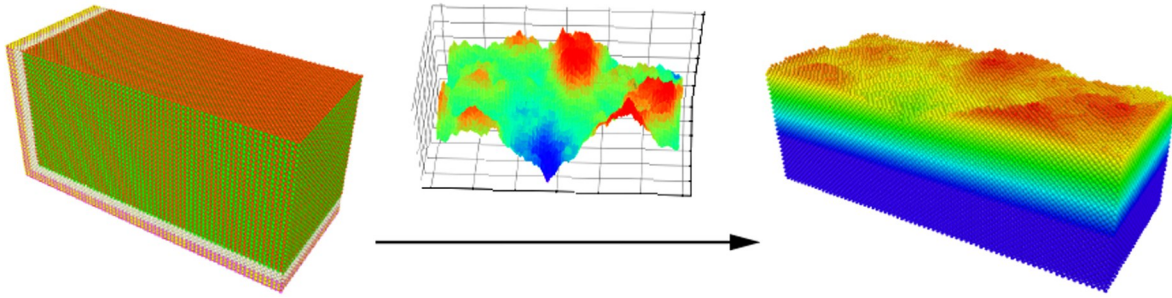


Fig.2 Generation process of surface with random roughness

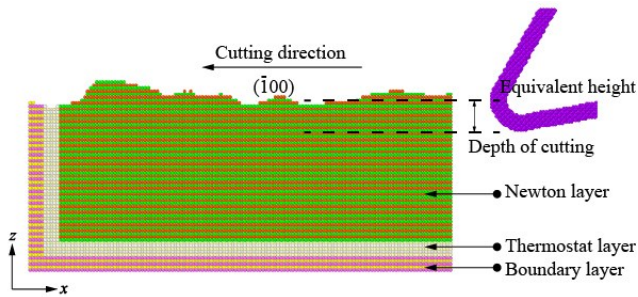


Fig.3 MD simulation model of nano-cutting process of γ -TiAl alloy

orientation is [001]. Table 1 shows the parameters of the cutter. Two tool rake angles of 30° and -30° were applied, which are the typical parameters of positive and negative rake angles of cutters. All types of tools have a uniform radius of 2 nm while the thickness of cutters in y -direction is 4 nm.

Table 2 shows the simulation parameters. Because the diamond is stiffer than γ -TiAl alloy, the cutter is considered as a rigid body. Once the atom coordinate file was imported, all the atoms were assigned at 300 K with the Gaussian distribution. Then the system was equilibrated at 300 K under the micro-canonical ensemble (NVE) for 50 ps. After the equilibration, the thermostat layer was set to the canonical ensemble (NVT), and then the tool moved at the speed of 100 m/s. As for the boundary condition, it is noted that the box size in x -direction and z -direction is long enough, so the

“p p p” boundary condition can be considered as the “f p f” condition. OVITO^[22] was also used for 3D visualization. The common neighbor analysis (CNA) was used to observe the lattice states and evolutions of stacking faults^[23].

1.4 Potential function

The accuracy of the potential function is critical to the effectiveness of the simulation. There are mainly two kinds of the potential functions in this research: embedded atom method (EAM) and Morse potential. EAM is widely performed in MD metallic systems^[24] and can be described as follows:

$$E = \sum_i F_i(\rho_i) + \frac{1}{2} \sum_{ij(i \neq j)} \phi_{ij}(r_{ij}) \quad (5)$$

$$\rho_i = \sum_{j(j \neq i)} f(r_{ij}) \quad (6)$$

where F_i is the embedding energy of atom i with an electron density ρ_i ; ϕ_{ij} represents the relative potential energy between atom i and atom j ; r_{ij} is the distance from atom i to atom j . The interaction between Ti-Ti, Ti-Al, and Al-Al was described by EAM function in Ref.[25]. The Morse potential is applied to describe the interaction between Ti-C and Al-C, as follows:

$$V(r) = D[1 - e^{-\alpha(r-r_0)}]^2 - D \quad (7)$$

where D is the intensity of action between two atoms, α represents the effective range, and r_0 is the equilibrium distance of two atoms. The parameters of Morse potential to describe Ti-C and Al-C are shown in Table 3^[26].

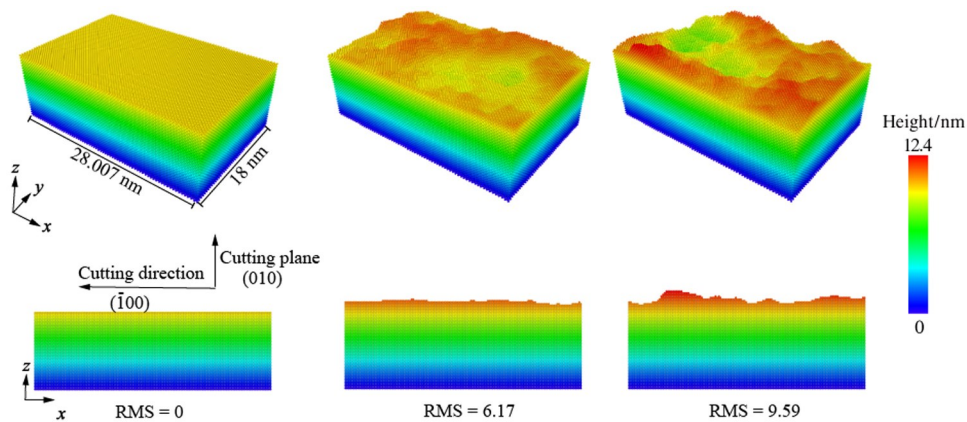


Fig.4 Simulated rough surface morphologies with different RMS values

Table 1 Geometric parameters of cutters

Parameter	Value
Tool radius/nm	2
Rake angle/(°)	-30, 30
Clearance angle/(°)	10
Thickness, y/nm	4
Height, z/nm	9
Width, x/nm	5

Table 2 Parameters of MD simulation

Parameter	Value
Tool material	Diamond
Cutting speed/m·s ⁻¹	100
Equivalent DOC/nm	1, 3
Equilibration step	50 000
Cutting step	200 000
Temperature/K	300
Boundary condition	P P P
Time step/ps	0.001

Table 3 Morse potential parameters of Ti-C and Al-C^[26]

Alloy	D/eV	a/nm^{-1}	r_0/nm
Ti-C	0.982	22.83	0.1892
Al-C	0.280	27.80	0.2200

2 Results and Discussion

The effects of DOC and angles of cutting edge of surfaces with different roughness were investigated under the condition of DOC varying from 1 nm to 3 nm, and the two types of rake angles were considered.

Fig. 5a–5c show the key cutting processes of simulated rough surface with RMS=6.17 when the equivalent DOC is 1 nm. The green part in Fig.5 represents the face-centered cubic (fcc) structure, the red part represents the hexagonal closest packed (hcp) structure, the blue part represents the body-centered cube (bcc) structure, and the white part represents the amorphous atoms. It should be noted that the tool of diamond structure is also colored by white, due to the auto CNA. The model is firstly equilibrated, and then the tool moves at a speed of 100 m/s. After the cutting process, the tool is deleted

and the model is relaxed again. In brief, the simulation is firstly equilibrated from 0 ps to 50 ps, then undergoes the cutting from 50 ps to 250 ps, and finally is equilibrated again from 250 ps to 300 ps. All the simulations were conducted based on this process.

2.1 Machining response of surface with different roughness

The rake angle of tools was set as 30°. Fig.6 shows a series of CNA snapshots during the cutting process with DOC=1 nm to study the defects nucleation and evolution. The fcc atoms were hidden for a better observation of defects. As the tool cuts the workpiece, the number of hcp and bcc atoms is increased. However, the large areas of stacking faults cannot be found because the cutting depth is too small.

In the case of RMS=0, 6.17, the trends of defect evolution are similar. At first, only a few isolated defective atoms are generated. The bcc atoms originate from the amorphous phase transition and the hcp atoms result from the nucleation before stacking fault formation. However, the stacking fault is difficult to form due to the small DOC. The stacking fault shortly forms and soon disappears in the cutting process, because the stacking fault is quickly released by the thermal activation energy. Finally, after the restoration of equilibration, the stacking fault is formed inside the chip again, which is derived from the amorphous atoms. The effects and evolution of roughness on cutting process are quite different with RMS=9.59. It is observed that the final stacking faults are formed at different positions and in different shapes. Due to the randomness of rough surfaces, it is difficult to analyze the specific defects using conventional theories. Therefore, the theories in Ref.[27] are adopted to explain the various phenomena.

The process of phase transformation can be divided into two categories in the nano-cutting process: contact-induced amorphization (CIA) and strain-induced phase (SIP) transformation. SIP transformation includes the strain-induced amorphization (SIA) and strain-induced ordered lattice change, while CIA usually contributes to the subsurface defects in the process of the chip formation and SIP transformation. The time distribution of the number of defective atoms is shown in Fig. 7. The number of defective atoms under the condition of RMS=9.59 can be explained by the following theory: the increased instantaneous DOC results in the increase in SIP region, which eventually leads to

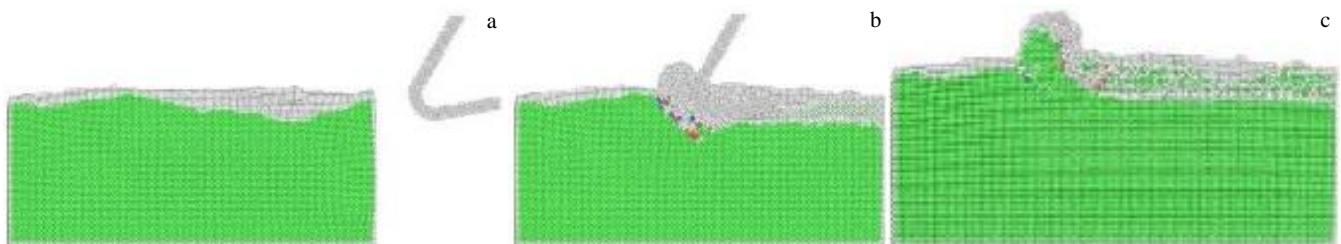


Fig.5 Cutting processes of simulated rough surface with RMS=6.17 and equivalent DOC of 1 nm: (a) equilibration; (b) initial cutting; (c) restoration of equilibration after cutting

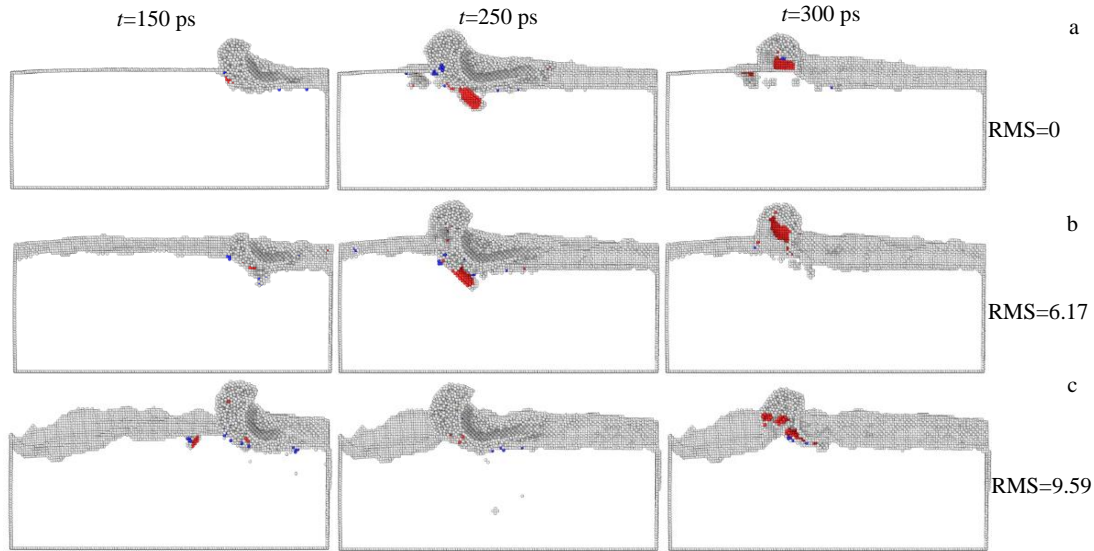


Fig.6 Material responses during nano-cutting of γ -TiAl alloy with DOC=1 nm and different surface roughness: (a) RMS=0, (b) RMS=6.17, and (c) RMS=9.59

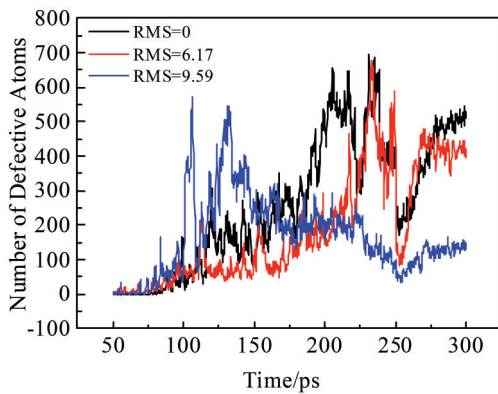


Fig.7 Time distribution of the number of defective atoms under different RMS conditions with DOC=1 nm

formation of more hcp atoms. However, the region of SIP is not large enough to generate the hcp atoms of sufficient size when the instantaneous DOC is small. Soon, due to the thermal activation effect, the defective atoms without enough size disappear. Hence, the groove on the surface plays an important role in the reduction of SIP region.

Besides, the stacking fault can also occur in CIA region after equilibration. When DOC is 1 nm, it can be observed that defective atoms in workpieces are mainly concentrated in the chips, as shown in Fig.6. However, the final stacking fault shows a large concentration characteristic under the conditions of RMS=0, 6.17, while that under the condition of RMS=9.59 is scattered and relatively small. It can also be explained by the surface groove. The fluctuation of surfaces generates less chips and finally results in fewer stacking faults. Hence, it can be concluded that under the condition of DOC=1 nm, CIA dominates the main region which is sensitive to the surface roughness; while the roughness has little effect on the number of defective atoms generated in SIP

region due to the obvious thermal activation effect, which thereby results in fewer defective atoms.

Fig. 8 displays the snapshots during cutting process under the condition of DOC=3 nm. It can be observed that more stacking faults are generated with increasing the value of DOC. At the initial cutting stage, more bcc atoms appear with increasing the roughness degree. According to Ref. [28], the number of bcc atoms can be considered as the degree of amorphous crystallization. Therefore, the large DOC leads to the expansion of CIA region and the formation of large-scale stacking faults at $t=250$ ps, as shown in Fig.8. However, due to the increase in DOC, the resultant large stacking fault cannot be released easily due to massive stacking faults.

Fig.9a shows the change curve of the number of defective atoms with time, while the number of defective atoms in the chip and on subsurface of the equilibrated workpieces is demonstrated in Fig.9b. It can be seen from Fig.9a that the curves under different roughness conditions show the similar trends compared with those in Fig. 7. However, the mechanisms are quite different. In Fig. 7, due to the small cutting depth, the effect of rough surface on the number of defective atoms is mainly concentrated in CIA region. When the cutting depth is 3 nm, the influence of rough surface can be observed in both CIA and SIP regions. The specific effect caused by roughness is related to the chip shape. It is noteworthy that when $t=250$ ps, the chip size becomes smaller with increasing the roughness. Meanwhile, the stacking faults with the same orientation are difficult to form due to the irregular shapes of chip. Hence, the new stacking fault is difficult to grow due to the relative stability of the system in chips, which is well presented in Fig.9b. The number of hcp and bcc atoms in the chip of the workpieces is decreased with increasing the surface roughness. It can also be seen that the defective atoms on subsurface are increased with increasing

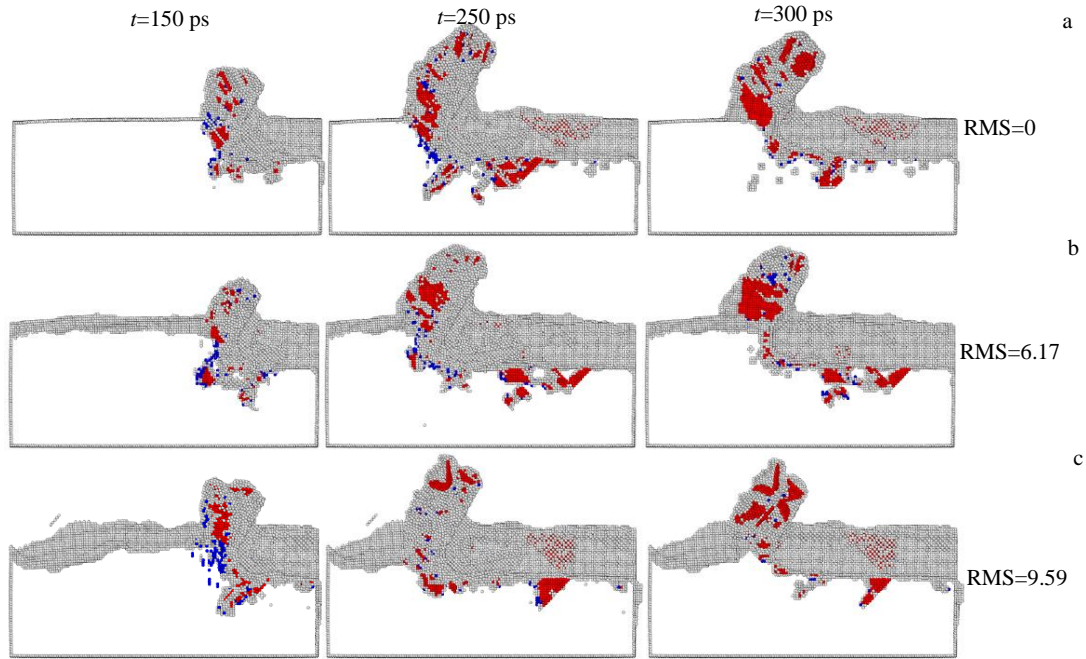


Fig.8 Material responses during nano-cutting of γ -TiAl alloy with DOC=3 nm and different surface roughness: (a) RMS=0, (b) RMS=6.17, and (c) RMS=9.59

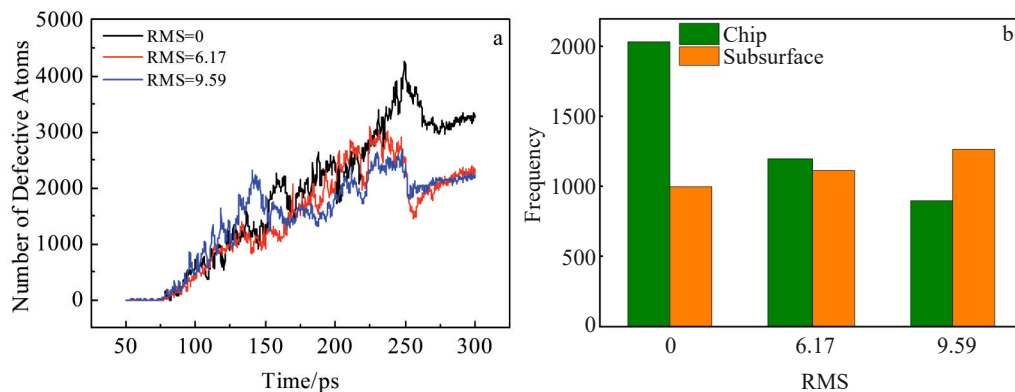


Fig.9 Time distribution of the number of defective atoms under different RMS conditions with DOC=3 nm (a); defective atom distribution in chip and on subsurface of equilibrated γ -TiAl alloys under different RMS conditions (b)

the surface roughness, because the large-scale stacking faults caused by the large instantaneous DOC cannot be easily released. The interactions between SIP and CIA regions determine the change trend of the number of defective atoms.

Fig. 10 shows the residual hydrostatic stress distributions before and after equilibration under the conditions of RMS=0, 9.59. It can be seen that the compressive stress exists below the cutter during the cutting process. However, the final compressive stress almost disappears after equilibration, due to the stress release after the tool is removed. It is worth noting that the residual stress distribution on chips is more disordered with increasing the value of RMS, which is consistent with the analysis results of the defective atom distribution. The larger the value of RMS, the more complex the atomic arrangement of the chip. In summary, the mechanisms of defect evolution are different when DOC is 1

and 3 nm. When DOC=1 nm, only the number of defective atoms in CIA region is greatly affected by the roughness. When DOC=3 nm, the effect of surface roughness on the number of defective atoms in SIP region becomes more obvious, and that in CIA region is also deeply affected by the roughness. Although the influence mechanisms are different, the increase in surface roughness will increase the defective atoms on the subsurface.

2.2 Analysis of cutting force and temperature

Fig. 11 shows the evolution of cutting force with RMS=0, 9.59 and different DOCs. Three phenomena need to be noticed: (1) with increasing the DOC, the cutting force also tends to increase; (2) when DOC=1 nm, the roughness can significantly reduce the normal cutting force rather than the tangential force; (3) as DOC increases, the effect of roughness on the normal cutting force is negligible. In brief, the effect of

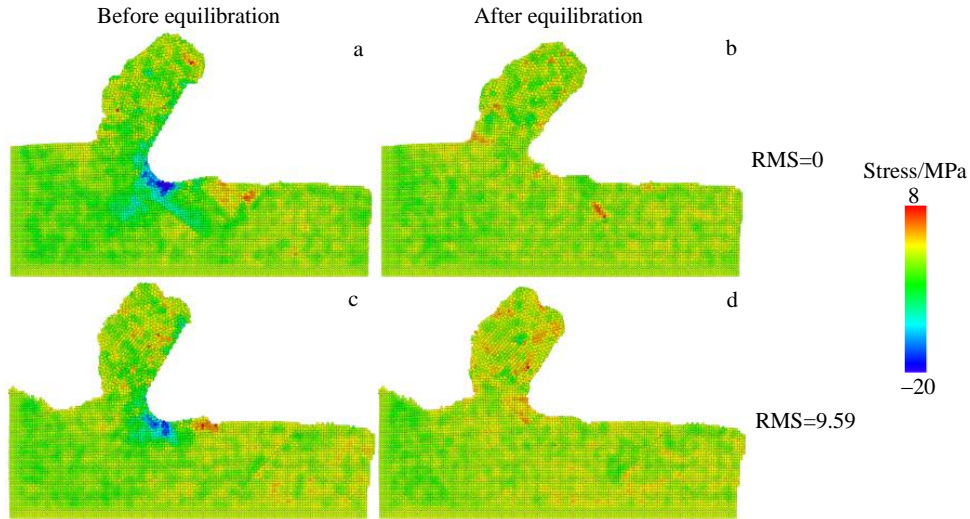


Fig.10 Residual hydrostatic stress distributions on different rough surfaces before and after equilibration: (a) RMS=0, $t=250$ ps; (b) RMS=0, $t=300$ ps; (c) RMS=9.59, $t=250$ ps; (d) RMS=9.59, $t=300$ ps

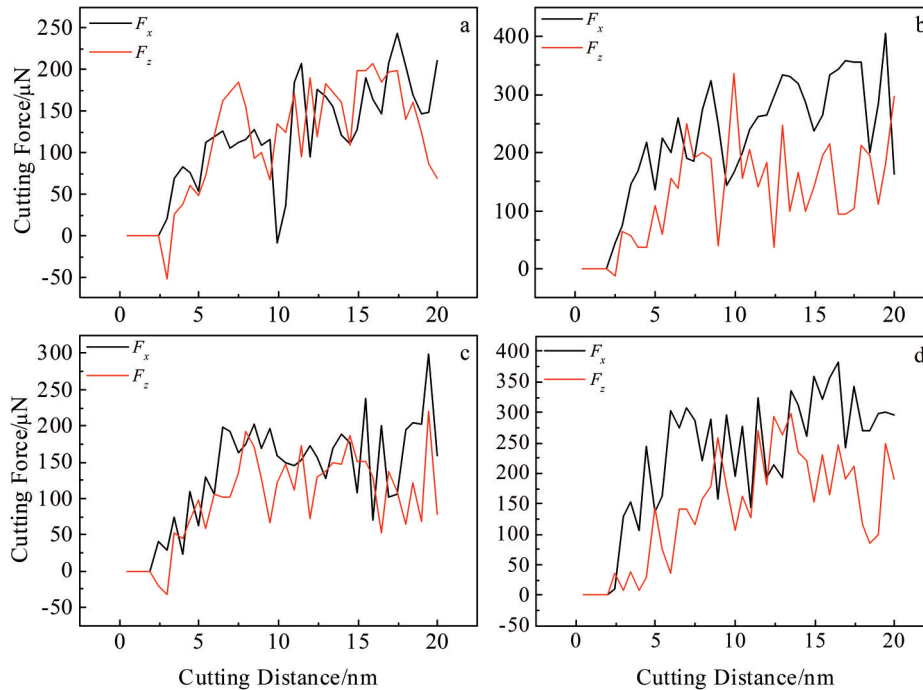


Fig.11 Cutting forces along different directions under different conditions: (a) RMS=0, DOC=1 nm; (b) RMS=0, DOC=3 nm; (c) RMS=9.59, DOC=1 nm; (d) RMS=9.59, DOC=3 nm

roughness becomes less obvious with increasing the cutting depth.

The average cutting forces under different conditions are shown in Fig.12. As shown in Fig.12, when DOC=1 nm, the difference between the cutting force along x -direction F_x and the cutting force along z -direction F_z is augmented with increasing the surface roughness. F_z is decreased obviously with increasing the roughness. However, when DOC=3 nm, the difference between F_x and F_z under different roughness conditions is negligible, because with increasing the DOC, the stable stacking faults begin to form, thereby increasing the

cutting force. Compared with the effects caused by stacking faults, the geometry effect is slight. In addition, when DOC=3 nm, the change trends of F_x and F_z are opposite. Because the surface roughness originates from the statistical data and the variation trend of F_x depends on the specific fractal condition of the surface, the specific change trend of cutting force is meaningless. However, the opposite trends of cutting forces at different cutting depths can reveal the qualitative conclusions. When DOC=1 nm, no stable stacking faults can be formed, as shown in Fig.6. The effect of SIP region is small, whereas the geometry of surface shows the crucial effect. The fluctuation

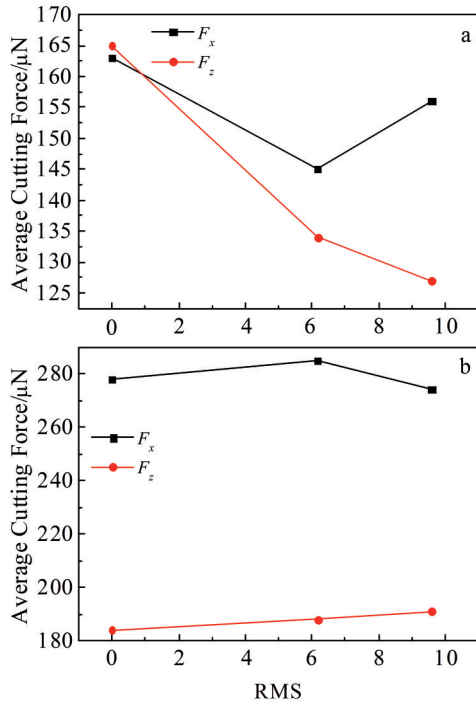


Fig.12 Average cutting forces F_x and F_z under condition of $\text{DOC}=1\text{ nm}$ (a) and $\text{DOC}=3\text{ nm}$ (b)

of instantaneous cutting depth results in the decrease in average cutting force F_z . In addition, when $\text{DOC}=3\text{ nm}$, the stacking faults are more obvious and can last longer on the subsurface, which leads to an increase in F_z when the tool cuts the subsurface. Meanwhile, the effect of surface geometry is no longer significant.

Fig.13 shows the average temperature of the cutting process under different cutting conditions. With increasing the DOC , the average temperature is increased almost linearly regardless of the roughness. However, due to the random surface fractals, the average temperature also changes randomly. Hence, the roughness cannot be used as a basis for temperature changes. Therefore, the surface fractal can influence the temperature of the cutting process, but the surface roughness will not have a qualitative influence on cutting temperature when DOC is increased from 1 nm to 3 nm .

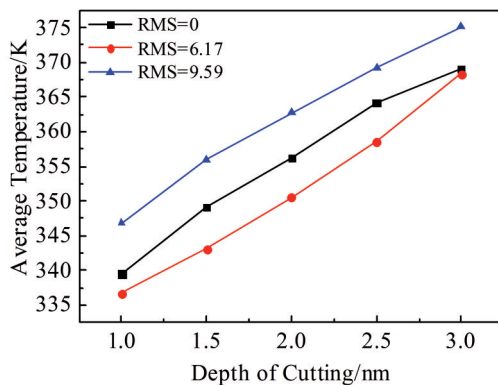


Fig.13 Average temperatures under different cutting conditions

2.3 Influence of rake angle

The rake angle is also considered during the simulations. Fig. 14 shows the snapshots of the residual defects of workpieces with different values of RMS and the rake angle of -30° . Under the condition of equivalent DOC of 3 nm , more subsurface defects are generated compared with that in Fig.8 (the rake angle is 30°). The fewer chip productions are due to the geometry of cutters. Fig.15 shows the number of defective atoms in chip and on the subsurface when the rake angle is -30° . It is obvious that the subsurface defects are much greater than those with the rake angle of 30° , because the rake angle of tools greatly changes the development of CIA region which should have formed the chips. The negative rake angle cutter pushes the amorphous atoms into the surface of the workpiece, and the high compressive stress leads to the phase transition mechanism dominated by SIP transformation. Hence, the larger SIP regions lead to more subsurface defects.

The number of subsurface defects under the condition of $\text{RMS}=9.59$ is more than that under $\text{RMS}=0$. The fewer the chips, the larger the SIP region; the larger the SIP region, the more defective atoms in subsurface. Meanwhile, the number

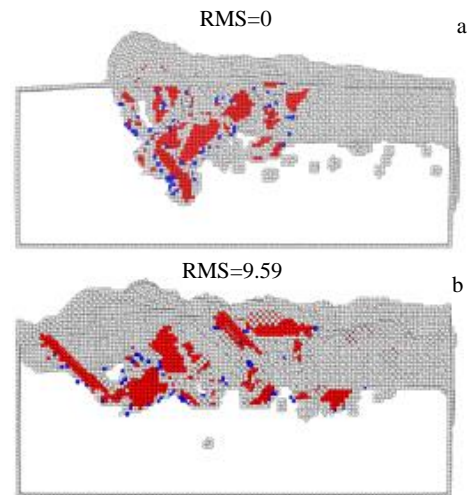


Fig.14 Residual defect distributions under the conditions of rake angle of -30° with $\text{RMS}=0$ (a) and $\text{RMS}=9.59$ (b)

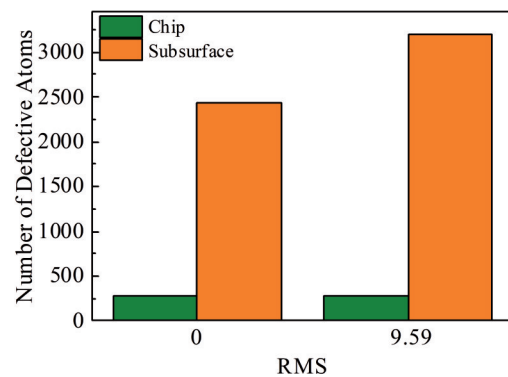


Fig.15 Number of defective atoms in different regions with $\text{RMS}=0, 9.59$ and rake angle of -30°

of defective atoms in chips is not sensitive to roughness, as shown in Fig.15, because the chip is always pressed into the surface and can never accumulate. Hence, when the tool stops moving and the workpiece begins to restore the equilibration, there is no difference in chip size of different workpieces.

3 Conclusions

1) When the cutting depth is 1 nm, only the effects caused by contact-induced amorphization (CIA) region are sensitive to the surface roughness. The effects caused by strain-induced phase (SIP) region in the cutting process are quickly released due to the thermal activation. Meanwhile, the scale of CIA region in the cutting process is decreased with increasing the surface roughness.

2) When the cutting depth is 3 nm, both CIA and SIP regions are important. However, with increasing the surface roughness, the number of defective atoms is decreased in CIA region, whereas that in SIP region is slowly increased. CIA region shows more obvious influence when the cutting depth is 3 nm.

3) The cutting force is decreased with increasing the cutting depth. Under the condition of shallow cutting depth, the surface shape has a great influence on the cutting force. However, with increasing the cutting depth, SIP region begins to dominate the influence on the cutting force. Besides, the surface fractals can influence the average temperature in the cutting process regardless of roughness with increasing the cutting depth from 1 nm to 3 nm.

4) Compared with that with a positive rake angle, the cutter with a negative rake angle can produce more defects in the cutting process. The increase in roughness can also increase the number of defective atoms on the subsurface of workpieces. The effects are more obvious when the cutter has a negative rake angle.

5) The surface roughness can affect the number of defects on the subsurface and in the whole alloy system. The increase in roughness can lead to the growth of defective atoms.

References

- Sommitsch C, Ionescu M, Mishra B et al. *Materials Science Forum*[J], 2016, 879: 113
- Bewlay B P, Nag S, Suzuki A et al. *Materials at High Temperatures*[J], 2016, 33(4): 549
- Castellanos S D, Cavaleiro A J, De Jesus A M P et al. *Proceedings of the Institution of Mechanical Engineers*[J], 2019, 233(3): 426
- Blackley W S, Scattergood R O. *Precision Engineering*[J], 1991, 13(2): 95
- Fang F Z, Xu F F. *Nanomanufacturing and Metrology*[J], 2018, 1(1): 4
- Ikawa N, Donaldson R R, Komanduri R et al. *CIRP Annals*[J], 1991, 40(2): 587
- Muhammad A, Zhang X Q, Mustafizur R et al. *International Journal of Machine Tools and Manufacture*[J], 2013, 64: 114
- Silling S A. *Journal of the Mechanics and Physics of Solids*[J], 2000, 48(1): 175
- An Minrong, Deng Qiong, Li Yulong et al. *Materials & Design* [J], 2017, 127: 204
- Zhu Zongxiao, Bin Peng, Feng Ruicheng et al. *Science China: Technological Sciences*[J], 2019, 62(11): 1916
- Zhang Lin, Zhao Hongwei, Guo Wenchao et al. *Optik*[J], 2014, 125(2): 682
- Saurav Goel, Andrii Kovalchenko, Alexander Stukowski et al. *Acta Materialia*[J], 2016, 105: 464
- Li Jia, Fang Qihong, Zhang Liangchi et al. *Computational Materials Science*[J], 2015, 98: 252
- Michail Papanikolaou, Konstantinos Salonitis. *Applied Surface Science*[J], 2019, 467: 309
- Ausloos M, Berman D H. *Proceedings of the Royal Society A*[J], 1985, 400(1819): 331
- Chubb S R, Papaconstantopoulos D A, Klein B M. *Physical Review B*[J], 1988, 38(17): 12 120
- Tang Fuling, Cai Houmin, Bao Hongwei et al. *Computational Materials Science*[J], 2014, 84: 232
- Liu Huaqiang, Qin Xuying, Ahmad Shakeel et al. *International Journal of Heat and Mass Transfer*[J], 2019, 145: 118 799
- David Avnir, Dina Farin, Peter Pfeifer. *Nature*[J], 1984, 308(5956): 261
- Steve Plimpton. *Journal of Computational Physics*[J], 1995, 117(1): 1
- Li Jianhua, Feng Ruicheng, Qiao Haiyang. *Metals*[J], 2019, 9(12): 1278
- Alexander Stukowski. *Modelling and Simulation in Materials Science and Engineering*[J], 2009, 18(1): 15 012
- Daniel Faken, Hannes Jónsson. *Computational Materials Science* [J], 1994, 2(2): 278
- Daw M S, Baskes M I. *Physical Review B*[J], 1984, 29(12): 6443
- Zope R R, Mishin Y. *Physical Review B*[J], 2003, 68(2): 24 102
- Zhu Ying, Zhang Yincheng, Qi Shunhe et al. *Rare Metal Materials and Engineering*[J], 2016, 45(4): 897
- Wang Jinshi, Zhang Xiaodong, Fang Fengzhou et al. *Applied Surface Science*[J], 2018, 455: 608
- Li Haiyan, Shao Zihao, Feng Ruicheng et al. *Philosophical Magazine*[J], 2021, 108(1): 38

γ -TiAl 合金纳米切削过程中随机表面粗糙度影响的原子模拟

冯瑞成^{1,2}, 杨晟泽¹, 邵自豪¹, 姚永军¹, 张 隽¹, 曹 卉¹, 李海燕^{1,2}

(1. 兰州理工大学 机电工程学院, 甘肃 兰州 730050)

(2. 兰州理工大学 数字制造技术与应用省部共建教育部重点实验室, 甘肃 兰州 730050)

摘 要: 采用分子动力学模拟方法研究了随机粗糙度对 γ -TiAl 合金纳米尺度切削的影响。为了模拟真实工件表面, 在考虑刀具不同前角和切削深度的情况下, 采用多参数的 Weierstrass-Mandelbrot (W-M) 函数生成随机表面粗糙度, 用工件的等效高度来量化切削深度。结果表明, 粗糙度对工件的纳米切削有不可忽视的影响。此外, 粗糙度的影响在不同切削参数的情况下也不同。

关键词: 分子动力学模拟; 纳米切削; W-M 函数; γ -TiAl 合金

作者简介: 冯瑞成, 男, 1976 年生, 博士, 教授, 兰州理工大学机电工程学院, 甘肃 兰州 730050, 电话: 0931-5135199, E-mail: postfeng@lut.edu.cn